

RESEARCH

Open Access



Visualization of HSP70-regulated mild-photothermal therapy for synergistic tumor treatment: a precise space-time mild-temperature photothermal ablation strategy

Binyue Zhang^{1,2†}, Yanchun Ma^{3†}, Qi Liu^{1†}, Shutong Wu¹, Lin Chen¹, Chunmei Jiang¹, Haonan Chen¹, Hongyan Jia^{2*}, Ziliang Zheng^{1*} and Ruiping Zhang^{1*}

Abstract

Mild-temperature photothermal therapy (MPTT) advances anticancer management by regulating reactive oxygen species (ROS) and lipid peroxides (LPO) to inhibit the overexpression of heat shock protein 70 (HSP70), thus decreasing the cellular heat resistance and increasing the efficacy of tumor ablation. However, formidable challenge remains on the traditional MPTT without imaging-guided optimal treatment time point, thus inadequate HSP70 blockage would potentially further diminish the effectiveness of MPTT. Herein, a novel biomimetic nanoprobe (Cu-ABTS@CCMs) is developed, based on encapsulating the multifunctional Cu nanoparticles and ROS-responsive 2,2'-azino-bis (3-ethylbenzothiazole-6- sulphonic acid) (ABTS) within cancer cell membranes (CCMs) to ensure second near-infrared photoacoustic (NIR-II PA) imaging-guided precise MPTT time point. The core Cu nanoparticles achieve highly effective HSP70 blockage via a nearly simultaneous cascade of photocatalytic O₂-generation and dual ROS/LPO accumulation. Triggered by self-enhanced ROS/LPO up-regulation, the ABTS can correspondingly oxidize to ABTS^{•+}, which further leads the real-time ratiometric PA signals (ABTS^{•+}-PA730/Cu-PA960) that show highly accurate visualization of ROS and quantitatively convert into dynamic tracking of the changes in HSP70 blockage. The intelligent dual-modality imaging information will provide more possibilities for the optimal time-point and site-specificity of MPTT and potential avenues for the development of clinical breast cancer treatments.

Keywords Dual-modal imaging, Ratiometric photoacoustic imaging, Second near-infrared window, Mild-photothermal therapy, Breast cancer

[†]Binyue Zhang, Yanchun Ma and Qi Liu contributed equally to this work.

*Correspondence:
Hongyan Jia
swallow_jhy@163.com
Ziliang Zheng
zzlsxty@sxmu.edu.cn

Ruiping Zhang
zrp_7142@sxmu.edu.cn

¹Laboratory of Molecular Imaging, Fifth Hospital of Shanxi Medical University (Shanxi Provincial People's Hospital), Taiyuan 030000, China
²Department of Breast Surgery, First Hospital of Shanxi Medical University, Taiyuan 030000, China
³Translational Medicine Research Center, Department of Pathology, Shanxi Medical University, Taiyuan 030001, China



Introduction

Breast cancer remains a major public health dilemma and the leading cause of mortality in women worldwide [1]. Triple-negative breast cancer (TNBC) is associated with non-specific diagnosis and unfavorable treatment due to the lack of well-defined molecular targets and high heterogeneity, resulting in lower overall survival (OS) among all subtypes [2]. Consequently, there is an urgent need for a specific therapeutic strategy in TNBC capable of precise lesion targeting and effective tumor growth inhibition. Inspiringly, PTT has become a promising therapy for clinical translation, not only because of its biologically noninvasive characteristics, accurate spatial-temporal specificity and minimal adverse effects [3, 4], but more importantly, it is highly controllable by converting light energy into heat energy to directly ablating the tumor [5, 6]. Especially, the second near-infrared (NIR-II, 1000–1700 nm)-mediated PTT has shown tremendous potential in precise diagnosis and effective treatment with more advantageous photothermal properties due to the deeper penetration (ca. 5–20 mm) and higher maximum permissible exposure (1.0 W/cm^2) [7–10].

However, conventional NIR-II PTT typically requires a temperature of at least $50 \text{ }^\circ\text{C}$ for complete tumor elimination. Such a high temperature and intense radiation will inevitably cause irreversible damage to the adjacent healthy tissues during tumor removal [11]. Encouragingly, the emergence of NIR-II mild-temperature PTT (MPTT, $< 45 \text{ }^\circ\text{C}$) not only maintain physiological and metabolic processes of normal tissues but also avoid severe heat destruction towards the vasculature nearby, which has overwhelmingly solved the bottleneck encountered by traditional PTT and promoted the relay delivery of therapeutic agents to the deep tumor [12]. Unfortunately, external hyperthermia stimuli would activate cellular innate self-protective response, such as HSP70 synthesis, to defense heat pressure [13]. During the treatment process, HSP70 guard cells from the aggregation of misfolded proteins caused by heat stress as well as promote the refolding, thus leading to cellular thermotolerance and the compromised therapeutic effects of MPTT [14]. Therefore, some small molecule HSPs inhibitors have been utilized, such as 17-AAG, gambogic acid, triptolide, STA-9090 to enhance the therapeutic effects of MPTT [15–18]. However, these inhibitors are unavoidably encumbered by impediments including poor solubility, pharmacokinetic uncertainty and increased complexity of drug synthesis, which seriously limit their clinical applications.

Alternatively, ROS and LPO provide novel tactics to cleave HSP70 at the source [19]. The ROS can destroy the cellular energy supply, thereby reducing protein biosynthesis. Additionally, LPO can spontaneously crosslink primary amines of proteins, leading to the destruction

of their structure and function [20]. Based on this, *Lin et al.* developed a single atom Pt nanozyme, which exhibited peroxidase (POD) and glutathione oxidase (GSHOx) mimicking activities, allowing ROS/LPO-boosted inhibition of HSPs for effective MPTT [21]. Our previous work reported a multifunctional nanoreactor, Ag-Cu@SiO₂-PDA/GOx (APG NRs), which cleaved HSP70 via both the generation of $\bullet\text{OH}$ and GOx-mediated energy shortage [22]. Regrettably, most available MPTT nanomedicines remain in an unstable “blind” mode regardless of whether photodynamic therapy/chemodynamic therapy (PDT/CDT) treatment reach the effective HSP70 inhibition efforts, leading to failure of further clinical applications. It is therefore imperative to develop a therapeutic agent with a visualization feature about HSP70 levels, offering a hopeful dynamic strategy to ensure the specific MPTT treatment time, making it a preferential choice for powerful integration of photothermal conversion capability with HSP70 silencing simultaneously.

Among various imaging techniques, photoacoustic imaging (PA) and fluorescence imaging (FL) in the NIR-II window have garnered significant attention for real-time and accurate imaging during the MPTT treatment process [23]. Especially, both NIR-II PA and NIR-II PTT share a similar scientific principle: the molecules absorb photons and undergo a quantum leap, and these highly unstable electrons return to a lower energy level, resulting in thermal conversion [24]. However, the conventional design concept of NIR-II PA nanoprobe being “always-on” in an intensity-dependent manner is insufficient for providing comprehensive space-time information effectively. Very recently, ratiometric PA detection has been reported as a promising alternative that remarkably enhances sensing specificity and sensitivity compared to simple PA signal detection [25]. For example, a smart nanozyme platform, consisting of MnOx, semiconducting polymer (PFODBT) and oxidase-responsive molecule (ORM), successfully sends back ROS level information through the simultaneous ratiometric signals output of dye molecular changes [26]. Nevertheless, addressing the considerable challenge of directly correlating ROS levels with HSP70 expression remains rare in order to establish exact quantitative relationships. Importantly, real-time visualization of HSP70 blockage offers a promising “MPTT therapeutic time zone (t_{MPTT})” for achieving precise space time mild-temperature photothermal ablation strategy.

Herein, we have developed an innovative exact quantitative relationship between ratiometric PA detection and HSP70 expression to establish the concept of “MPTT therapeutic time zone (t_{MPTT})”. This is achieved by utilizing the multi-nanozyme capability of Cu-ABTS@CCMs nanoprobe (CAC NPs) within tumor microenvironment (TME) that simultaneously realizes accurate tumor

localization and timing. The “all-in-one” CAC NPs were first fabricated, in which the monodisperse spherical Cu-based nanoparticles were modified with ROS-responsive 2,2'-azino-bis (3-ethylbenzothiazole-6-sulphonic acid) (ABTS) and then CAC NPs effectively coated 4T1 breast cancer cell membranes (CCMs) (Scheme 1). Based on the specific tumor targeting ability of CCMs, the CAC NPs efficiently reach the tumor region rapidly and exhibit superior POD-like and GSHOx-like enzyme activity, simultaneously enhancing $\cdot\text{OH}$ generation and GSH reduction. This leads to oxidative stress in cells, resulting in LPO and mitochondrial dysfunction, ultimately depleting ATP levels and causing HSP70 degradation to overcome heat resistance. Moreover, the CAC NPs ensure a stable increase in the PA signal at 960 nm (PA_{960}) without bleaching from any photophysical or chemical interferences. The ROS-sensitive molecule ABTS can be oxidized into $\text{ABTS}\cdot^+$, which exhibits strong and distinct absorption at 730 nm (PA_{730}). Remarkably, the ratiometric PA signals ($\text{PA}_{730}/\text{PA}_{960}$) would be greatly helpful to dynamic and accurate monitoring of HSP70 expression, thereby determining the optimal NIR switching time.

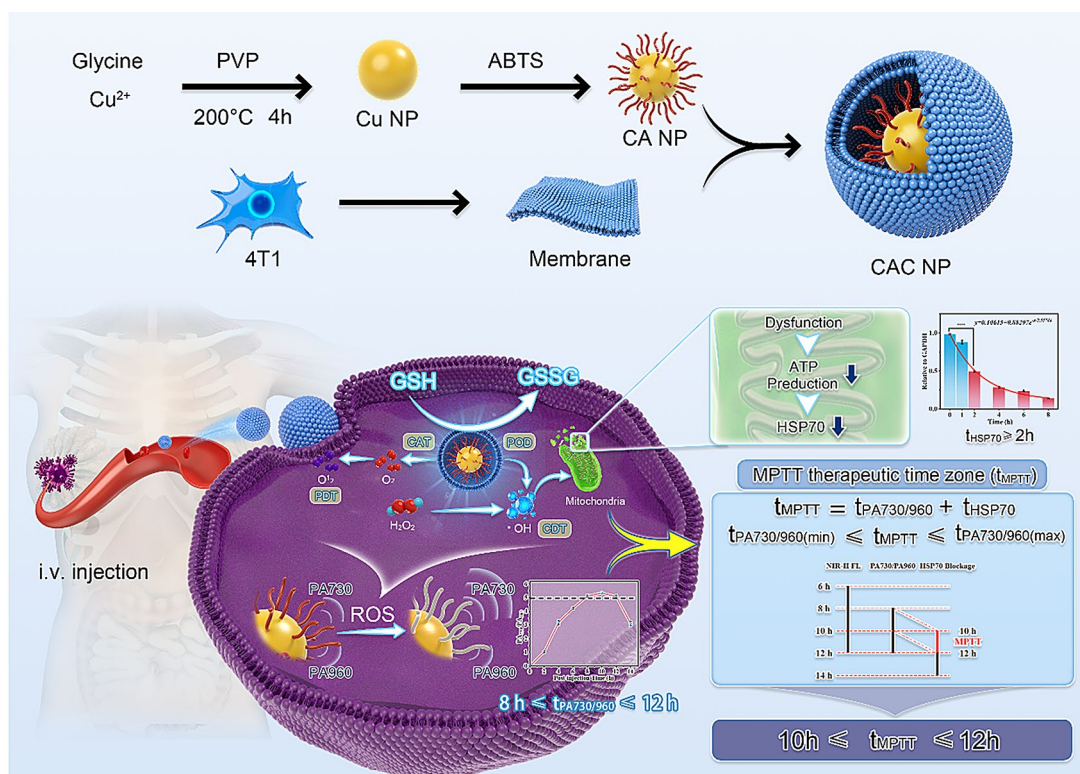
Experimental section

Materials and experimental details are provided in the Supporting Information. All animal studies were performed in Animal Experiment Center of Shanxi Medical

University and the procedures involving experimental animals were in accordance with protocols approved by the Institutional Animal Care and Use Committee of the Animal Experiment Center of Shanxi Medical University (No. 2016LL141, Taiyuan, China).

Results and discussion

General synthetic routes of Cu-ABTS@CCMs nanoprobes (CAC NPs) were shown in Scheme 1. Monodisperse ABTS-loaded Cu nanoparticles were initially synthesized through a facile hydrothermal strategy using glycine and PVP as co-reductants, then encapsulated in 4T1 cancer cell membranes to obtain the biomimetic CAC NPs. Transmission electron microscopy (TEM) images clearly demonstrated that all the CAC NPs had a spherical morphology with an average particle size ranging from 22.5 to 28.5 nm (Fig. 1a). As shown in Fig. 1b, the successful encapsulation was directly visualized by high-magnification TEM image, in which CAC NPs were observed with a thickness of 7–9 nm outer cell membrane shell. Importantly, taking advantage of the enhanced permeability and retention (EPR) effect, the CAC NPs with unique spatial structure and size can passively enter the tumor through interendothelial gaps along the blood vessel wall and effectively accumulate in the tumor region [27, 28]. Elemental mapping analysis demonstrated the uniform presence of Cu, O, and N in



Scheme 1 Schematic diagram of the synthesis process of the CAC NPs and the mechanism that establishes an innovative exact quantitative relationship between ratiometric PA detection and HSP70 expression to establish the concept of “MPTT therapeutic time zone (t_{MPTT})”

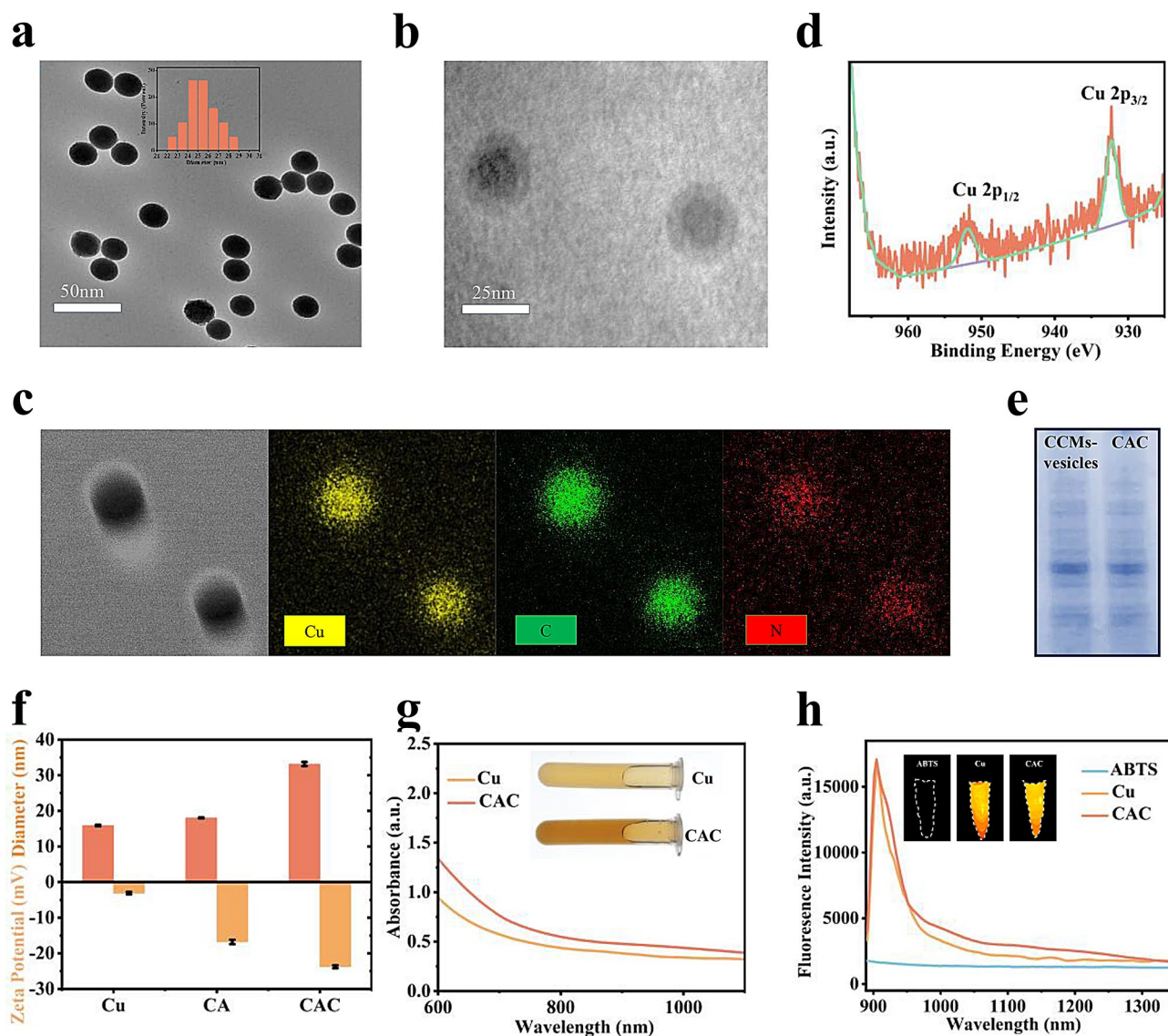


Fig. 1 Synthesis and characterizations of CAC NPs. **(a)** Representative low-magnification TEM image of CAC NPs (scale bar:50 nm). Inset: TEM-measured size distribution of CAC NPs. **(b)** High-magnification TEM image of CAC NPs (scale bar: 25 nm). **(c)** Elemental mappings of CAC NPs. **(d)** Cu 2p XPS spectra in CAC NPs. **(e)** SDS-PAGE protein analysis of CMM-vesicles and CAC NPs. **(f)** The hydrodynamic sizes and zeta potential of Cu, CA, CAC NPs. **(g)** Absorption of Cu, CAC NPs (inset: solubility of ABTS, Cu, and CAC). And **(h)** fluorescence spectra of ABTS, Cu, CAC NPs (inset: fluorescence images of ABTS, Cu, and CAC at 1064 nm, respectively.)

the CAC NPs (Fig. 1c). Additionally, X-ray photoelectron spectroscopy (XPS) analysis was performed to determine the elemental chemical valence of the CAC NPs (Fig. 1d). The binding energy peaks at 952.08 eV and 932.28 eV correspond to Cu 2p_{1/2} and Cu 2p_{3/2} respectively, revealing that the primary species of Cu was Cu⁰ [29]. During preparation, the membrane vesicles from 4T1 cells were purified using a combination of membrane dissociation and differential speed centrifugation techniques coated onto CA. Coomassie brilliant blue staining on SDS-PAGE gel verified successful translocation of cell membrane onto the cores (Fig. 1e). The coating process with the cell membrane resulted in a change in mean diameter

for the CAC NPs from 18.0 ± 0.52 to 33.1 ± 0.84 nm, as observed by dynamic light scattering (DLS). Meanwhile, the zeta potential value of -23.79 mV for CAC NPs was higher than that (-16.79 mV) observed for CA (Fig. 1f). Importantly, the CAC NPs exhibited remarkable stability in physiological media, remaining unaggregated for up to 72 h in various solutions without significant changes observed in the DLS and zeta potentials (Figure S1). And the CAC NPs also showed good solubility in aqueous media. The UV-Vis absorption spectrum of CAC NPs exhibited a broad range of absorption from 600 to 1200 nm, indicating their potential for efficient light absorption in the NIR-II window crucial for enhancing

the PA imaging and PTT performance (Fig. 1g). Furthermore, Fig. 1h showed that compared with Cu nanoparticles there was no obvious fluorescence weakening and quenching in the NIR-II fluorescence intensity of CAC NPs while maintaining a consistent fluorescence peak position. Based on these characteristics, CAC NPs could be used for biological imaging in the NIR-II region to reduce tissue autofluorescence and scattering emission, which in turn enable deeper penetration depth, providing a solid foundation for further biomedical applications.

Motivated by the obvious absorption in the NIR-II region, we evaluated the photothermal capability of CAC NPs upon NIR-II laser treatment in an aqueous solution. As seen in Fig. 2a, the temperature could achieve 43.7 °C at a low concentration (500 µg/mL) after 5 min (1064 nm, 0.75 W/cm²). The CAC NPs demonstrated concentration-dependent which aligned with the requirements of MPTT. Additionally, various power intensities of the 1064 nm laser ranging from 0.25, 0.5, 0.75, and 1.0 W/cm² were employed to irradiate the CAC NPs (Fig. 2b).

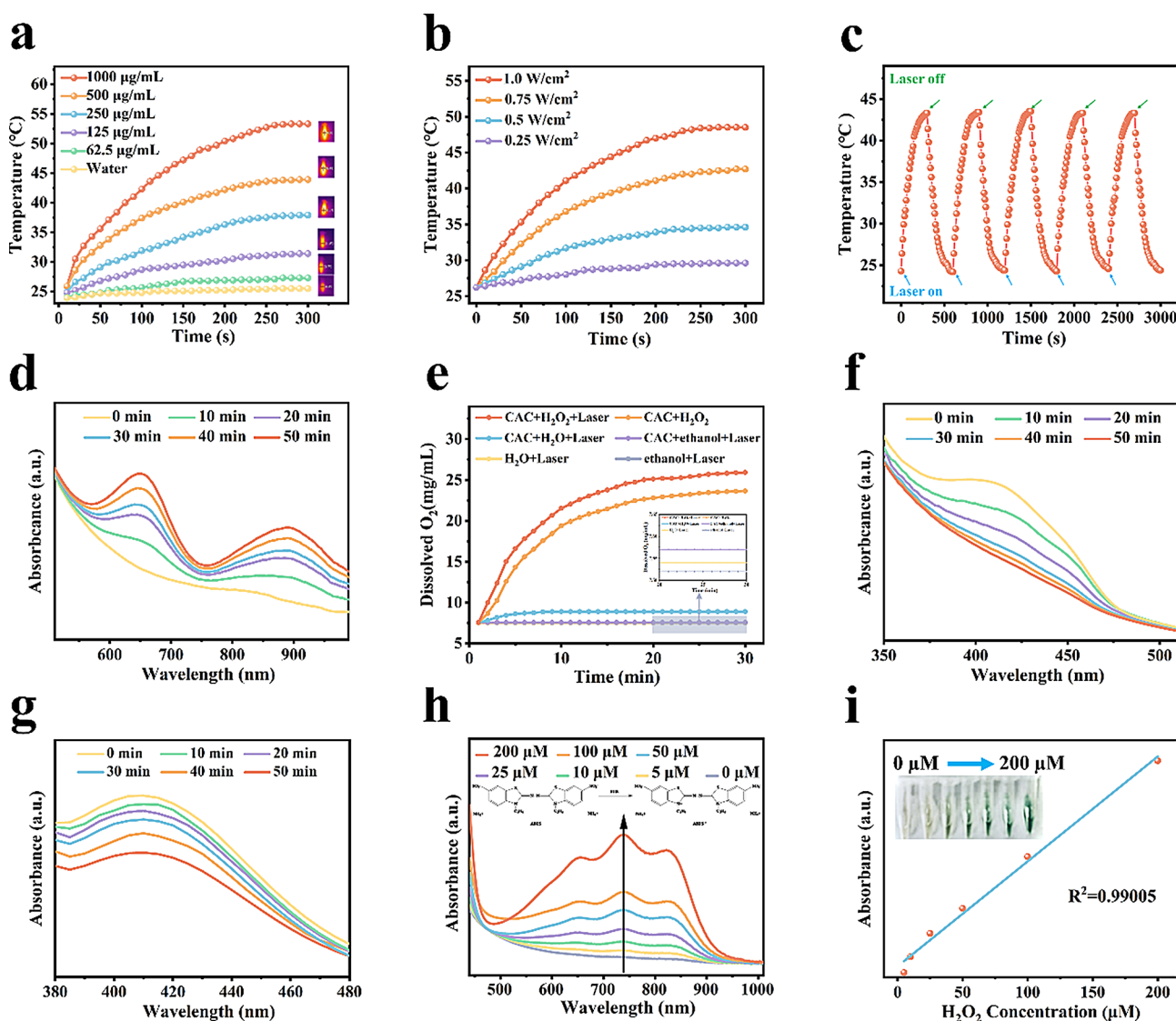


Fig. 2 (a) Temperature changes of CAC NPs at varying concentrations (0, 62.5, 125, 250, 500, and 1000 µg/mL; 0.75 W/cm²). Inset: Infrared thermal images of CAC NPs dispersion. (b) Temperature change curves of CAC NPs solutions (500 µg/mL) after irradiation with 1064 nm NIR laser at different powers for 5 min. (c) Photothermal stability of CAC NPs solution (500 µg/mL) upon 1064 nm NIR laser irradiation for five on/off cycles (0.75 W/cm²). (d) TMB was used to detect the fluorescence intensity change curve of ·OH produced by CAC NPs solution (500 µg/mL) at different time. (e) Oxygen-evolving curves of CAC NPs (500 µg/mL) in various conditions (CAC + H₂O₂ + Laser, CAC + H₂O₂, Cu + H₂O + Laser, Cu + ethanol + Laser, H₂O + Laser, and ethanol + Laser). (f) Absorbance spectra of DPBF treated with the CAC NPs (500 µg/mL) upon 1064 nm laser irradiation. (g) Absorbance spectra of DTNB treated with the CAC NPs (500 µg/mL). (h) The UV-Vis absorption spectra of CAC NPs (500 µg/mL) before and after different concentrations of H₂O₂ treatments (0–200 µM). Inset: Chemical structure and responsive mechanism of ABTS toward ABTS⁺. (i) The NIR fluorescence emission at various H₂O₂ concentration (inset: corresponding emission intensity excited at 1064 nm as a function of different concentrations)

Similarly, higher laser irradiation powers led to elevated temperatures of the CAC NPs. With the optimal concentration and irradiation power determined, we subsequently conducted five consecutive “ON-OFF” cycles to evaluate both temperature elevation curve and absorption profiles of CAC NPs. As illustrated in Fig. 2c, no noticeable reduction in the rate of temperature rise was observed, indicating superior photothermal stability. Thus, the CAC NPs hold great promise as a photothermal agent for PTT in the NIR-II window and provided strong support for further exploration of their catalytic ability-induced MPTT.

The designed CAC NPs could provide a “one enzyme and one laser, multi-function and enhanced therapy” strategy to greatly increase the intracellular ROS generation, providing an optimistic approach for cleaving HSP70 and achieving the efficient therapeutic paradigm toward MPTT. To confirm the production of $\cdot\text{OH}$ from the CAC NPs POD-like enzyme, 3,3',5,5'-tetramethylbenzidine (TMB) was employed as an indicator probe. As depicted in Fig. 2d, a substantial increase in absorption peaks is observed upon incubation of oxidized TMB (oxTMB) with CAC NPs over a period of 50 min, suggesting that the core Cu-nanoparticles catalyzed cytotoxic $\cdot\text{OH}$ generation from H_2O_2 . Specifically, the CAC NPs exhibit not only intrinsic CAT-like activity but also demonstrate photocatalytic performance for water splitting into O_2 under one NIR-II light irradiation (Fig. 2e), thereby achieving dual-catalytic hypoxia alleviation and promoting nearly simultaneous cascade of type-II PDT. As expected, after introducing laser irradiation (1064 nm), obvious amounts of O_2 were generated in the CAC aqueous solution compared to the ethanol solution. Moreover, a substantial release of O_2 was observed in the CAC + H_2O_2 + laser group, indicating its efficient O_2 supplementation. To evaluate the production capacity of another highly biotoxic ROS via the CAC NPs, 1,3-Diphenylbenzofuran (DPBF) was employed as a $^1\text{O}_2$ indicator. Figure 2f demonstrated a continuous decay curves for DPBF within 50 min, confirming the excellent ability of CAC NPs to produce $^1\text{O}_2$. Additionally, apart from its remarkable $\cdot\text{OH}/^1\text{O}_2$ production capacity, the CAC NPs exhibited glutathione peroxidase-like (GSHox) activity by consuming reducing agents GSH. The total GSH level was quantified using 5,5'-dithiobis-(2-nitrobenzoic acid) (DTNB), which measure UV absorbance at 412 nm corresponding to the formation of 5-thio-2-nitrobenzoic acid (TNB). A gradual decrease in TNB UV absorption indicated that the CAC NPs-mediated catalysis can achieve the integration of ROS enhancement and GSH depletion (Fig. 2g). This process facilitated the ROS accumulation within the tumor region. Collectively, these observations demonstrate that the CAC NPs can serve as

robust nanoprobe for combined tumor therapy involving MPTT/PDT/CDT with enhanced ROS generation.

The loading chromogenic substrates ABTS experienced rapid oxidation into photo-sensitive counterpart $\text{ABTS}\cdot^+$ upon exposure to generated ROS concentration in the TME. To validate the significant responsiveness of ABTS to catalysis by CAC NPs, UV-vis absorption spectra were measured before and after the addition of H_2O_2 . As displayed in Fig. 2h, there was a substantial enhancement in absorption at 730 nm for the CAC NPs, accompanied by a color change from colorless to dark green. This response exhibited a linear dependence with a certain H_2O_2 concentration (0-200 μM) (Fig. 2i). In addition, with a fixed concentration of 100 μM H_2O_2 , time-dependent changes in absorption at 730 nm were observed (Figure S2). These increased curves at 730 nm and standard UV-Vis absorption spectrum demonstrated that the CAC NPs could be employed as a reliable NIR-II ratiometric nanoprobe for rapid and quantitative detection of ROS fluxion during clinical breast cancer therapy.

Encouraged by the excellent promising physicochemical properties, we aimed to explore the “all-in-one” anti-tumor performance of CAC NPs in vitro. Before that, NIR-II FL imaging was used to intuitively visualize the cellular uptake of CAC NPs in 4T1 cells treated with CA NPs and CAC NPs (500 $\mu\text{g}/\text{mL}$). As depicted in Fig. 3a, the significant higher NIR-II fluorescence intensity of CAC NPs -treated cells at different time exhibited more rapid accumulation and more specific retainment at the tumor cells relative to CA group. This phenomenon indicated that the CAC NPs camouflaged by breast cancer cell membranes exhibited enhanced drug delivery and excellent cell homologous-targeting capabilities, which was mainly attributed to the homologous adhesion nature triggered by surface antigens [30–32]. Next, the cytotoxicity of CAC NPs was evaluated using the Cell Counting Kit-8 (CCK-8) on human umbilical vein endothelial cells (HUVEC). It was evident that a negligible dark cytotoxicity of CAC NPs was observed even at the concentration up to 500 $\mu\text{g}/\text{mL}$ (Figure S3), suggesting good biocompatibility. As a sharp contrast, concentration-dependent cytotoxicity was observed in the 4T1 cell viability a 1064 nm laser irradiation (0.75 W/cm^2) for 5 min (Fig. 3b). Such great therapeutic effect could be ascribed to the photo-sensitive responsive process that efficiently promoted MPTT/PDT/CDT synergistic therapeutic effect.

In order to identify the antitumor capabilities involved in the CAC NPs-mediated “one enzyme and one laser, multi-function and effective MPTT” strategy, N-acetylcysteine (NAC, the precursor of glutathione) was employed as an effective ROS scavenger and ice bath was applied to minimize interference from heat generation [33]. Cell viability was quantified when the cells were

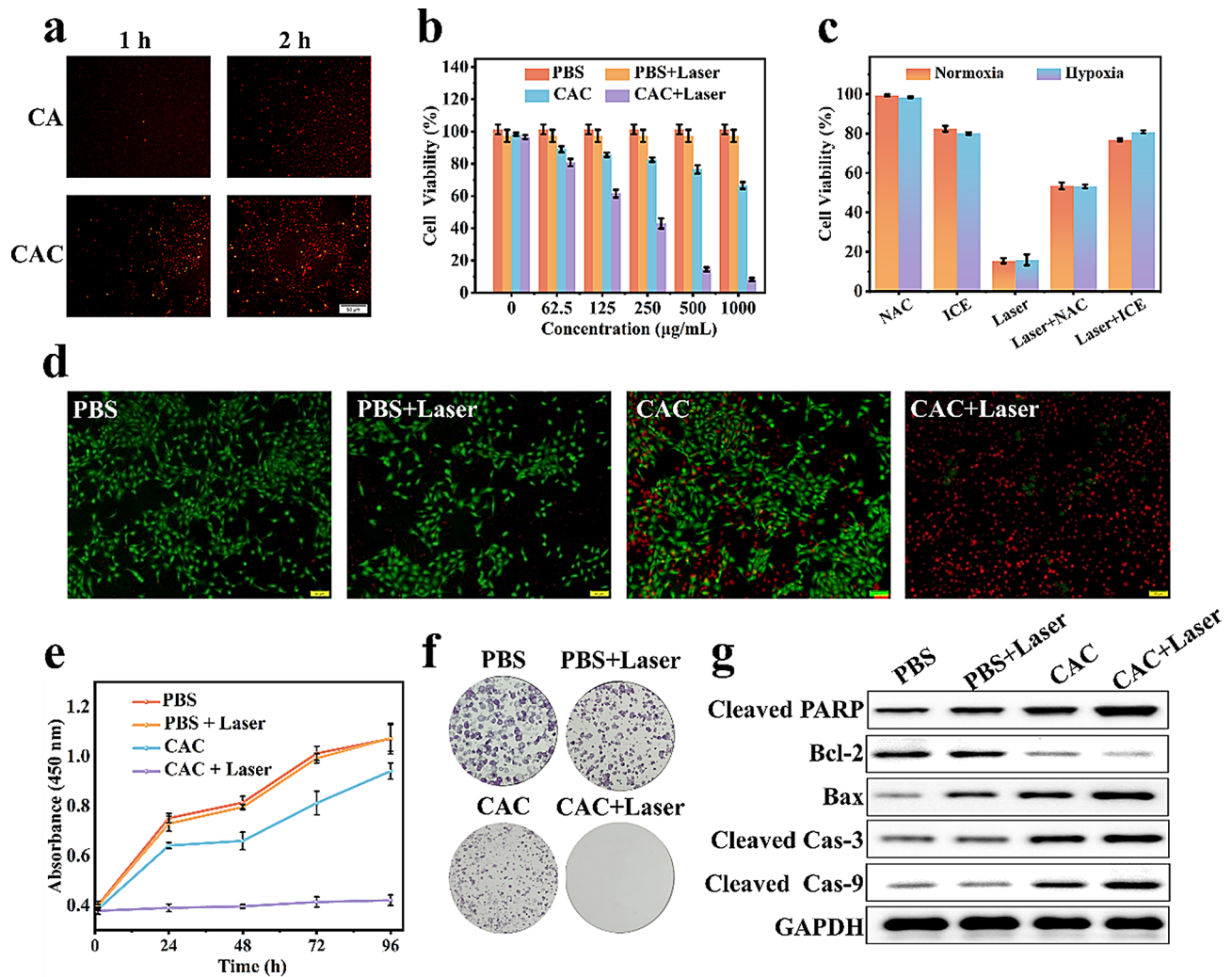


Fig. 3 (a) NIR-II fluorescence images of 4T1 incubated with CA and CAC NPs (500 µg/mL) during different periods (1 and 2 h). (b) Cell viability of 4T1 cells after treated with different groups (PBS, PBS + Laser, CAC, CAC + Laser). (c) Cytotoxicity evaluation of CAC NPs (500 µg/mL) in 4T1 cells under different conditions. (d) Calcein AM/PI double staining in 4T1 cells cultured with different conditions: PBS, PBS + Laser, CAC, CAC + Laser. Concentration (CAC NPs) = 500 µg/mL. (e) The growth curves of 4T1 cells were subjected to different treatments at 500 µg/mL. (f) Colony formation assay of 4T1 cells with different treatments. (g) Western blot assays of 4T1 cells to detect the expression of the apoptotic-related proteins after different treatments. Scale bar: 50 µm

cultured with CAC NPs (500 µg/mL) and treated with NAC, ICE, Laser, Laser + NAC, or Laser + ICE under both normoxic and hypoxic conditions, respectively. In comparison to CAC NPs + Laser + NAC (53.4%), a greater proportion of cells were damaged in CAC NPs + Laser + ICE (76.3%) under normoxic conditions (Fig. 3c), suggesting that the PTT-induced modality was more effective in terms of superior synergistic antitumor efficacy. Furthermore, the cell viability of the CAC NPs + ICE group was 82.4%, whereas the viability in the CAC NPs + Laser + ICE group (76.3%) was just lower slightly. The results revealed that the enhanced ROS generation was mainly benefited from the intrinsic CDT potency. Similar results were demonstrated by Calcein Acetoxymethyl Ester /propidium iodide (Calcein AM/PI) staining, compared to the

other treatment groups, the CAC NPs + Laser groups exhibited strong red fluorescence from PI, which demonstrated a significant CDT/PDT/MPTT synergistic therapeutic effect (Fig. 3d). To comprehensively explore the long-term therapeutic efficacy of the CAC NPs-mediated synergistic strategy in vitro, the growth curve, colony formation, and apoptosis-associated proteins were analyzed. Meanwhile, the cell proliferation was detected with various treatments at 500 µg/mL every 24 h. We get the same results in Fig. 3e, the inhibition of cell proliferation with CAC NPs + Laser group was the strongest among all groups, indicating the CDT/PDT/MPTT synergistic therapeutic effect. Of note, colony formation assays (Fig. 3f) further intuitively emphasized increased growth inhibition and decreased colony-forming ability in CAC

NPs + Laser group. In addition, western blot of proteins was performed to understand the profound pathways underlying CAC NPs-mediated 4T1 cell apoptosis. Acting as a facilitator of the mitochondrial apoptotic pathway, the expression of proapoptotic protein Bax was significantly up-regulated in the combined therapy group (CAC NPs + Laser) [34]. Meanwhile, the downstream proteins including caspase-3, caspase-9, and PARP were cleaved and active, which finally played an essential role in the mitochondrial cell apoptotic pathway (Fig. 3g). Taken together, the above results provided compelling evidence that the CAC could be employed as an activatable NIR-II FL nanoprobe to efficiently eradicate tumor cells via “one enzyme and one laser, multi-function and effective MPTT” strategy.

It has been demonstrated that the CAC NPs exhibited a powerful tumor cell-killing effect in mimic tumor micro-environment via a synergistic MPTT/PDT/CDT strategy; however, its potential mechanism remained unclear. Typically, excessive ROS was considered to be associated with intracellular oxidative stress damage, leading to mitochondrial dysfunction and extensive protein synthetic obstruction, ultimately proceeding to cell apoptosis or necrosis [35]. As the precursor step of enhanced PDT, the dual cellular O₂ production of CAC NPs was detected by an O₂ probe [(Ru(dpp)₃)]Cl₂ whose fluorescence can be quenched through the O₂ accumulation. It has been observed in Fig. 4a and Figure S9 that the 4T1 cells treated with CAC NPs + Laser exhibited the weak red fluorescence signals in comparison with the other groups due to oxygen deprivation mitigation. While H₂O₂ was added, a much higher degree of fluorescence quenching demonstrated not only photocatalytic performance for water splitting into O₂ but also intrinsic CAT-like activity, which would benefit subsequent PDT therapy. To further verify the potential PDT properties of CAC NPs upon NIR-II laser irradiation, the singlet oxygen sensor green (SOSG) reagent was utilized to detect ¹O₂ level (Fig. 4b and c, ****P* < 0.001). As expected, the CAC NPs + Laser group induced enhanced intracellular ¹O₂ generation, clearly confirming the excellent sensitization of PDT. Secondly, •OH generation of CAC NPs-mediated POD-like enzyme activity could achieve timely tumor elimination in a specific-localization manner to improve the efficacy of breast cancer. We then assessed the intracellular •OH level using 3′(p-hydroxyphenyl) fluorescein (HPF). As displayed in Fig. 4d and e, the activated HPF signal were accompanied with the high-profile CDT efficacy in the CAC NPs and CAC NPs + Laser groups, confirming the excellent •OH generation (****p* < 0.001). Moreover, CAC NPs-mediated various mechanisms therapy all resulted in a substantial amount of ROS, which was measured with a 2′,7′-dichloro-dihydro-fluorescein diacetate (DCFH-DA) probe, emitting green fluorescence after being oxidized.

The higher fluorescence intensity in the CAC NPs + Laser group revealed the excellent intracellular ROS production (Fig. 4f and g), which was the underlying mechanism to achieve timely tumor cells apoptosis and successor cellular protein HSP70 blockage to finally realize tumor excision and enhanced MPTT (****p* < 0.001).

Over the ROS generation period, oxidation-reduction imbalance triggers biomembranes LPO and the dynamic sabotage of cellular physiological, biochemical, immune reactions, ultimately achieving tumor cell apoptosis. Herein, the intracellular LPO was detected by the green fluorescent dye 4, 4-difluoro-5-(4-phenyl-1,3-butadienyl)-4-bora-3a,4a-diaza-s-indacene-3-undecanoic acid (C11-BODIPY581/591). As can be seen in Fig. 4h and S4, in comparison to control, the green fluorescence intensity in CAC NPs + Laser group increased sharply, powerfully demonstrating the generation of LPO resulted from the CAC NPs. Secondary to this cytosolic damage is the dysfunction of prominent cell energy factory, mitochondria, producing ATP through aerobic respiration to maintain normal protein synthesis [12]. As illustrated in Fig. 4i, a gradual decline in the ATP level of 4T1 cells was observed after 2 h following CAC NPs treatment, suggesting a highly toxic aggression to 4T1 cells (****p* < 0.001). The probe 5,5′,6,6′-tetrachloro-1,1′,3,3′-tetraethylbenzimidazolyl carbocyanine-iodide (JC-1) was further used to stain intracellular mitochondrial membrane potential (MMP) dysfunction at different treatments, with red fluorescence in healthy mitochondria and transformation to green fluorescence in pathological mitochondria. In accordance with the level of ATP shortage, the MMP was nearly entirely depleted in cells subjected to CAC treatment for 2 h, which indicated that the highly biotoxic ROS and LPO had a powerful impact on mitochondria function (Fig. 4j and S5). Furthermore, as shown in the bio-TEM images of Fig. 4h, compared with control groups, mitochondrial ultrastructural damage began to appear in the cells after coculture for 2 h, characterized by enlargement, swelling, and vacuolar degeneration. Such physiological disorder and structural damage confirmed that the CAC-induced ROS and LPO ultimately led to irreversible mitochondria-mediated apoptosis and offered possibility for the heat resistant protein HSP70 inhibition in MPTT.

Based on the above therapeutic performance analysis, it is reasonable to speculate that CAC NPs could regulate MPTT owing to the HSP70 inhibition by ROS/LPO generation and ATP starvation, which provided a potential candidate for time-point MPTT strategy in vitro. The relationship between different CAC NPs coculture-times and subsequent HSP70 blockage was analyzed by western blot (Fig. 5a and b, ****p* < 0.001). In parallel with the ATP deficiency, the intracellular HSP70 level was decreased sharply at 2 h and then the decline rate

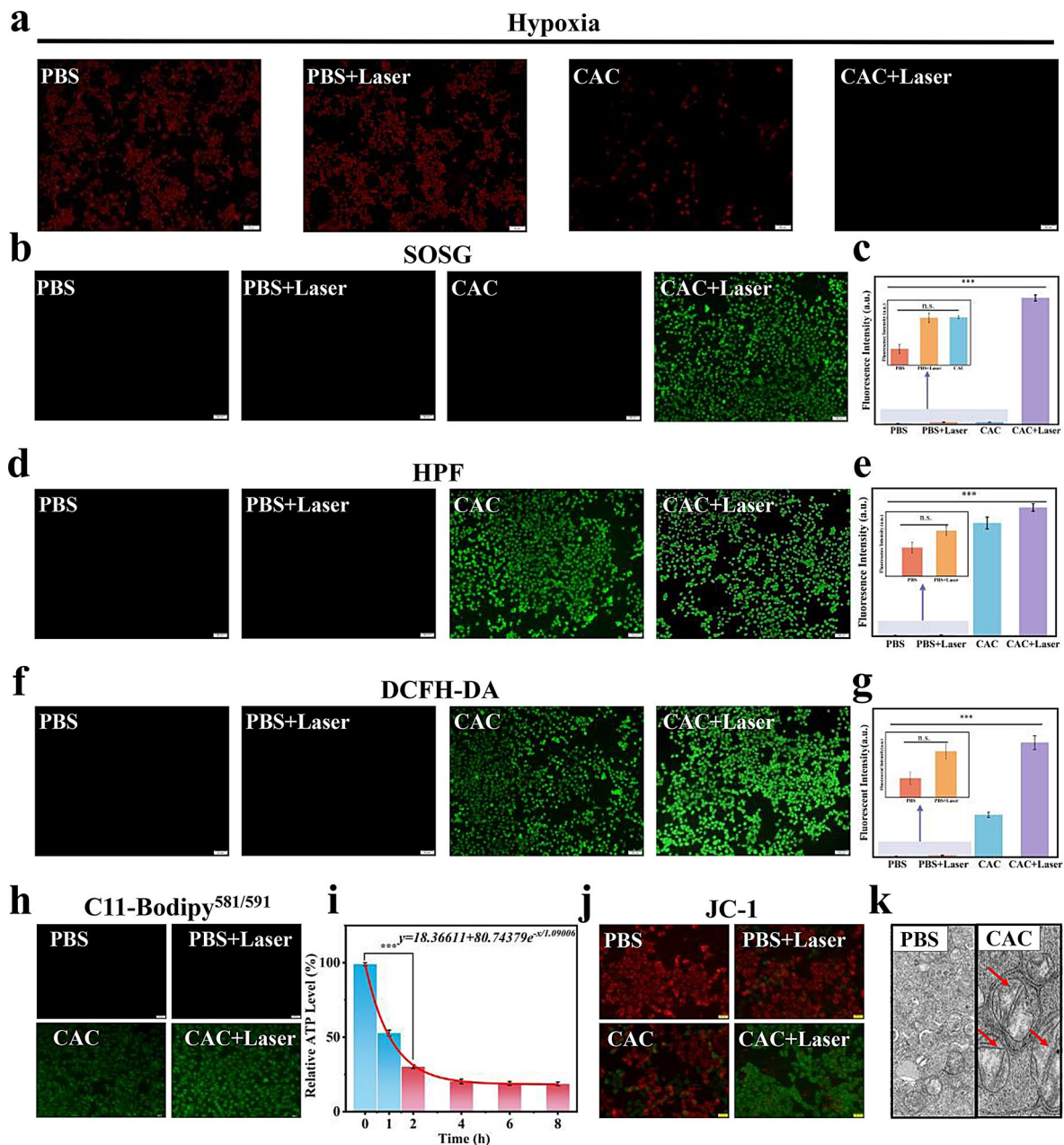


Fig. 4 (a) The production of oxygen determined by quenched RDPP fluorescence in different conditions. Concentration (CAC NPs) = 500 $\mu\text{g}/\text{mL}$. Fluorescence analysis of (b, c) SOSG detecting intracellular $^1\text{O}_2$, (d, e) HPF detecting intracellular $\cdot\text{OH}$, and (f, g) intracellular ROS detection in 4T1 cells cultured with different conditions: PBS, PBS + Laser, CAC, CAC + Laser Concentration (CAC NPs) = 500 $\mu\text{g}/\text{mL}$. h) LPO level in 4T1 cells treated with various formulations measured by C11-BODIPY581/589 fluorescent dye (CAC NPs) = 500 $\mu\text{g}/\text{mL}$. i) Intracellular ATP levels at different time points after CAC + Laser treatment (CAC NPs) = 500 $\mu\text{g}/\text{mL}$. j) Mitochondrial membrane potentials of 4T1 cells determined by JC-1 assay after different treatments. (CAC NPs) = 500 $\mu\text{g}/\text{mL}$. k) Bio-TEM images of cells treated with PBS and CAC+Laser. Red arrows mark the damaged mitochondria (down). Scale bar: 50 μm . * $p < 0.05$, ** $p < 0.01$, *** $p < 0.001$

tended to be gentle. This indicated that the CAC NPs has caused ROS/LPO accumulation, ATP shortfall, and mitochondrial damage after treatment for 2 h, which in turn resulted in HSP70 synthetic difficulties, and this may be the best time for NIR-II “ON” to realize MPTT. To further investigate the MPTT cytotoxicity under different culture time, a CCK-8 assay was conducted and the result

in Fig. 5c showed that the cell viability decreased with the prolongation of coculture time and a half maximal inhibition was consistent with the HSP70 downregulation around 2 h (** $p < 0.001$). Accordingly, these findings indicated that 2 h with CAC NPs treatment could be the shortest time to effectively decrease HSP70 levels and activate NIR-II MPTT ($\Delta t_{\text{HSP70}} \geq 2 \text{ h}$) via ROS/LPO

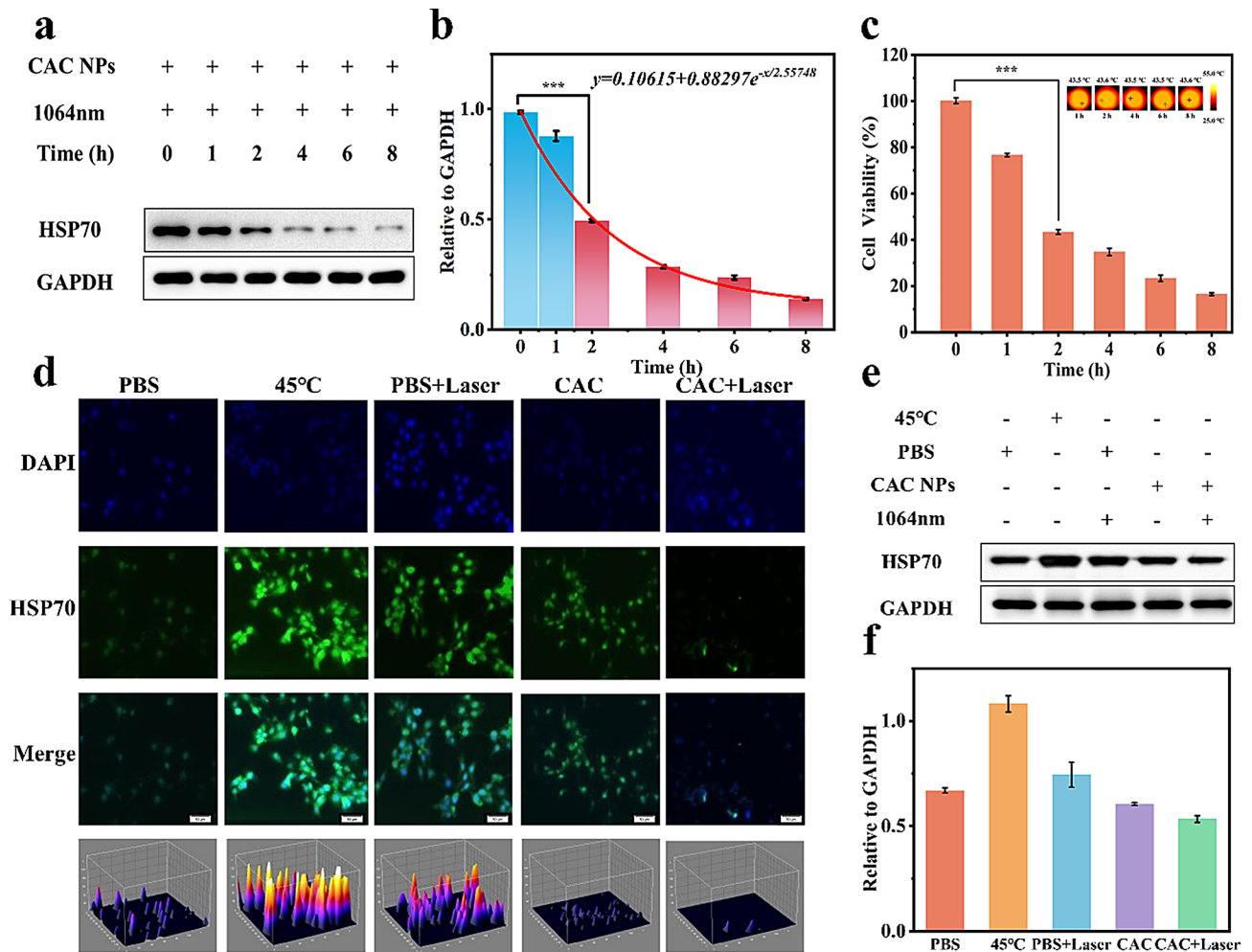


Fig. 5 (a, b) Western Blotting detection of the expression of HSP70 at different time points after CAC+Laser treatment (CAC NPs) = 500 $\mu\text{g}/\text{mL}$. (c) Cell viability at different time points after CAC+Laser treatment (CAC NPs) = 500 $\mu\text{g}/\text{mL}$, with an inset of cells temperature images. (d) The immunofluorescence staining of HSP70 with different treatments at 4 h. (CAC NPs) = 500 $\mu\text{g}/\text{mL}$. (e, f) Western Blotting detection of the expression of HSP70 with various treatments at 4 h. Scale bar: 50 μm . * $p < 0.05$, ** $p < 0.01$, *** $p < 0.001$

accumulation-mitochondria dysfunction-energy supplement disorders, which were further confirmed by a series of experiments in vitro. As shown in immunofluorescence images (Fig. 5d), the CAC NPs + Laser-treated 4T1 cells exhibited a greater HSP70 inhibition at 2 h, since ATP deficiency could effectively activate the intracellular protein synthesis system malfunction. The HSP70 level was also analyzed by western blot and showed a same distinct decrease due to ATP inadequacy (Fig. 5e and f). These results provided further evidences that the CAC NPs could dynamically weaken the heat-induced HSP70 expression after the sufficient treatment time (≥ 2 h), thereby achieving an excellent MPTT therapy efficiency. Thus, CAC NPs presented a novel prospect for dynamic MPTT therapy through mitochondria dysfunction-mediated HSP70 blockage.

Real-time information of ROS generation in vivo was extremely critical to achieve highly effective

imaging-guided successful HSP70 blockage and MPTT therapy against breast cancer, as the key feature to obtain precise localization and optimal NIR-II treatment time point in clinical application. Encouraged by the stable NIR-II absorption, emission, and ultrasensitive responsiveness towards ROS in vitro, the CAC NPs were intravenously injected into breast cancer-bearing mice to provide intelligent integration of dual-modality imaging guidelines. As shown in Fig. 6a, the NIR-II FL signal emerged rapidly at the site of the breast cancer after 2 h injection distinguish the breast cancer region from normal tissue. Quantitative analysis revealed that the intensity of NIR-II FL signals continuously increased over time and demonstrated a high signal-to-noise ratio (SNR) over a period of 6–12 h (Fig. 6b), illustrating the effective delivery and productive interval of CAC NPs into tumors. Ex vivo fluorescence imaging further revealed that the CAC NPs accumulated mainly in tumors, followed by

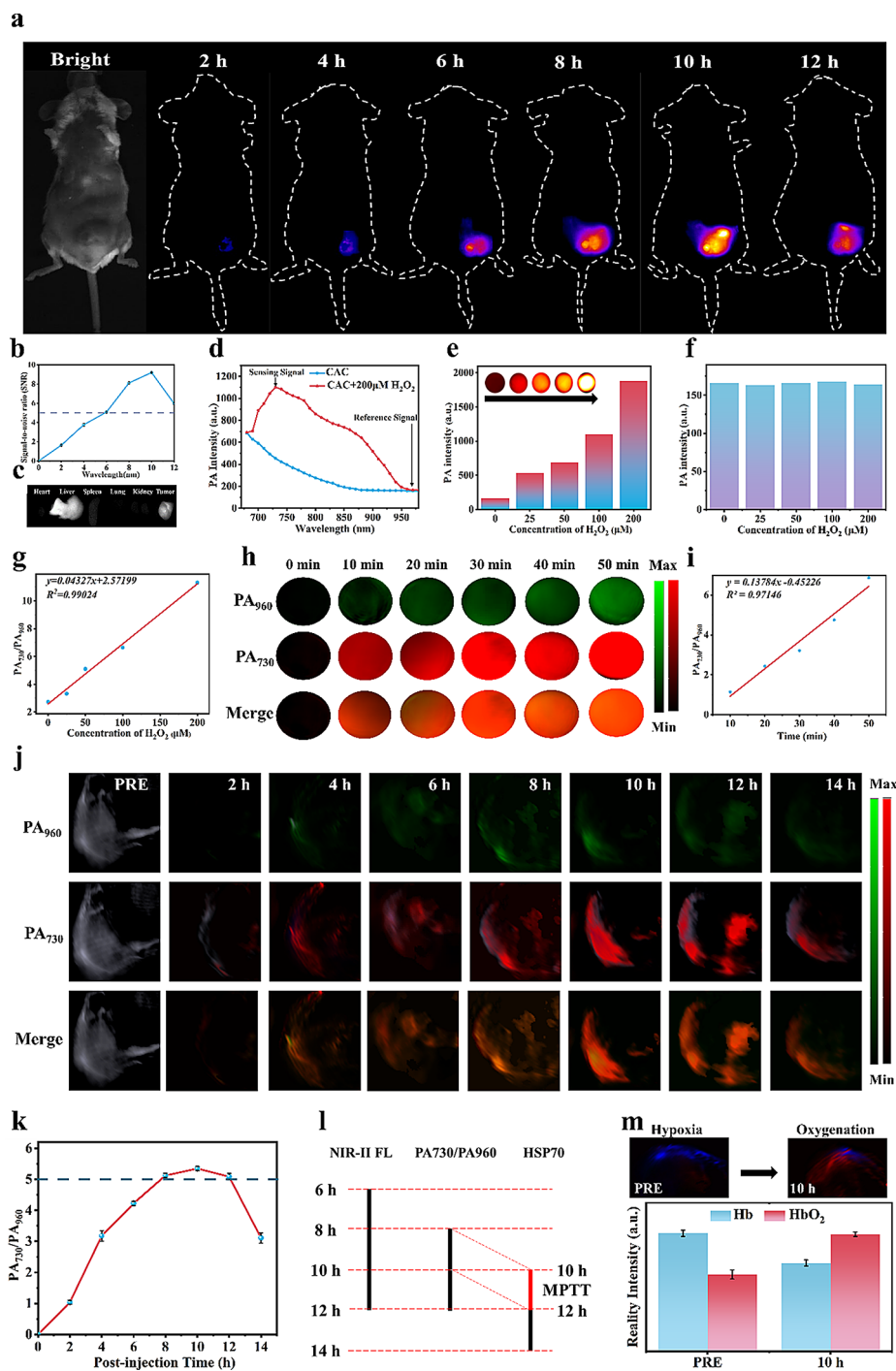


Fig. 6 (a) Time-dependent NIR-II FL imaging of 4T1 tumor-bearing mice after intravenously injected with the CAC NPs (10 mg/kg 200 μ L). (b) Time-dependent signal-to-noise ratio (SNR) changes determined by the NIR-II FL imaging of mice after CACNPs treatment. (c) NIR-II FL images of excised major organs and tumor from 4T1 tumor-bearing mice treated with the CAC NPs. In vitro (d) PA spectrum of CAC NPs before and after H₂O₂ treatments (200 μ M). (e and f) PA signal intensity of CAC NPs at 730 nm and 960 nm with different H₂O₂ treatments (0–200 μ M), with an inset of PA images. (g) The PA₇₃₀/PA₉₆₀ ratio of the CAC NPs as a function of the concentration of H₂O₂ in PBS. (h) The change of PA images at 960 and 730 nm after the CAC NPs solution treated with 100 μ M H₂O₂ (from right to left). (i) PA₇₃₀/PA₉₆₀ signal ratios of CAC NPs measured under different time after 100 μ M H₂O₂ treatment. In vivo (j) representative PA images at 960 and 730 nm of tumors in 4T1 tumor-bearing mice after intravenous injection of CAC NPs at different post-injection times. (k) The ratiometric PA signals (PA₇₃₀/PA₉₆₀) in the tumor as a function of postinjection time of CAC NPs. (l) Schematic illustration of “MPTT therapeutic time zone (t_{MPTT})”. (m) Representative PA images of 4T1 tumors to determine the tumoral oxygenation status by measuring the ratios of oxygenated hemoglobin ($\lambda = 850$ nm) and deoxygenated hemoglobin ($\lambda = 750$ nm) after the CAC NPs at 14 h post-injection. A 1064 nm laser irradiation (0.75 W/cm², 5 min) was performed at tumor region after 10 h injection

the liver, reflecting the possible metabolism pathway of hepatic-intestinal clearance (Fig. 6c).

Superior hyperthermia performance and ultrasensitive responsiveness of ABTS towards ROS in vitro gave CAC NPs the potential to become a ratiometric PA imaging probe in vivo. As shown in Fig. 6d, the responsive properties towards ROS of CAC NPs were investigated using PA imaging after simulating the TME with 100 μM H_2O_2 . A strong PA intensity peaks at 730 nm was almost consistent with post-reactive CAC UV-vis spectra, while an overlap occurred at 960 nm. In addition, the sensing signal at 730 nm increased sharply in a H_2O_2 concentration-dependent manner, while the reference signal at 960 nm remained largely unaltered (Fig. 6e and f). Considering the linear correlation between the signal intensity ratio of $\text{PA}_{730}/\text{PA}_{960}$ and H_2O_2 concentration ranging from 0 to 200 μM (Fig. 6g), we were derived that CAC NPs could functionally imply ROS accumulation at the tumor sites. Accordingly, in vitro ratiometric PA imaging was further performed for time-related quantitative measurement of ROS generation (Fig. 6h). In comparison to PA signals stability at 960 nm, the PA signals at 730 nm ascribed to ABTS oxidation gradually increased over time. A positive linear correlation gave the potential to guide the suitable time point in vivo (Fig. 6i). Taken together, it is reasonable to construct that CAC NPs could be employed as a reliable ratiometric nanoprobe for rapid, quantitative detection of ROS-mediated cellular physiological activities.

To achieve clinical translation, appropriate MPTT treatment time point was necessary to realize maximum therapeutic effect, consisted of the sufficient ROS accumulation in tumor sites ($t_{\text{PA730}/\text{PA960}}$) and the complete blockage of HSP70 expression in cells (Δt_{HSP70}). Due to the excellent responsive properties, balb/c mice bearing breast cancer were injected intravenously (*i.v.*) with CAC NPs to investigate dynamic therapy and obtain intelligent information about ROS generation. As shown in Fig. 6j, the PA960 (Pseudo green) increased gradually over time, reached a plateau at 6 h and declined rapidly mainly due to hepatic metabolism after post-injection 12 h. As a sharp contrast, a significant signal increase at 730 nm (Pseudo red) was clearly observed in the tumor region with high speed until its plateau was achieved at 10 h (Figure S6). Accordingly, quantitative analysis revealed that at 8–12 h the $\text{PA}_{730}/\text{PA}_{960}$ ratio exhibited a high sensing signal-to-reference noise ratio, reaching a maximum peak of 5.34 ± 0.06 at the 10 h post-injection, which was ≈ 5.18 -fold higher than that of the 2 h post-injection (1.03 ± 0.07) (Fig. 6k), suggesting $\text{PA}_{730}/\text{PA}_{960}$ ratio could effectively guide the synergistic CDT/PDT/MPTT therapy in breast cancer. Besides, the loaded ABTS were rapidly oxidized into $\text{ABTS}^{\bullet+}$ in PA_{730} and directly pointed ROS level. Consequently,

combining the time point of HSP70 blockade in cells ($\Delta t_{\text{HSP70}} \geq 2$ h) with the most efficacious time zone of $\text{PA}_{730}/\text{PA}_{960}$ ratio ($t_{\text{PA730}/\text{PA960}} = 8 \sim 12$ h), the MPTT may be optimized to achieve antitumor efficacy between 10 and 12 h post-injection (Fig. 6l). Such specific “MPTT therapeutic time zone (t_{MPTT})” not only visualized the enhanced ROS generation in tumors but also highlighted the ability to achieve highly-effective clinical imaging-guided precise treatment in the future.

Furthermore, since tumor hypoxia could weaken the ROS-mediated CDT/PDT/MPTT efficacy, we investigated the oxygenation capability of CAC NPs by detecting the signals of oxygenated and deoxygenated hemoglobin (HbO_2 and Hb) at different wavelengths of 850 and 750 nm in tumors. After 10 h post injection, apparent PA signal of HbO_2 (red) was visualized, alongside a reverse alteration in the Hb signal (blue), which may be linked to the direct dual-catalytic O_2 generation by CAC NPs in situ, further alleviating the hypoxic TME and benefiting the subsequent ROS generation (Fig. 6m).

Encouragingly, the precise time zone of aforementioned imaging-guided therapy ($t_{\text{MPTT}} = t_{\text{PA730}/\text{PA960}} + \Delta t_{\text{HSP70}}$) motivated us to further evaluate the antitumor performance of CAC NPs in vivo at a random time point. Once tumor volume reached 100 mm^3 , the breast cancer-bearing mice were randomly divided into four groups (PBS, PBS + Laser, CAC NPs, CAC NPs + Laser), and then treatment was administered every 2 days via intravenous injection as well as NIR irradiation was given at 12 h post-injection to trigger prominent MPTT. The IR thermal imaging and temperature changes of tumor sites were captured (Fig. 7a). As shown in Fig. 7b, the CAC NPs group achieved a final temperature of around 45 $^{\circ}\text{C}$, which met the requirements for MPTT. Over the next 14 days, the physical images of mice were recorded in Fig. 7c, and it was obvious that the tumor volume of the CAC NPs + Laser exhibited much greater inhibition while that of the PBS group kept growing rapidly (Fig. 7d). Such stark contrast was mainly attributed to the suitable time point of NIR-II exposure which activated powerful MPTT. Additionally, the results of the tumor weight also confirmed these findings (Fig. 7e). Furthermore, no significant body weight loss was detected in all these four groups (Fig. 7f), displaying the good biocompatibility of CAC NPs. Additionally, the survival curve of the remaining mice also confirmed that the CAC NPs + Laser group had a longer survival time, indicating that the CAC NPs + Laser group could effectively inhibit the growth of breast cancer and prolong the survival time which was the key to clinical translation (Fig. 7g).

Moreover, to further validate the effect of ROS-mediated synergistic CDT/PDT/MPTT therapy on tumor tissue, we prepared frozen sections from freshly obtained tumor tissue and conducted Dihydroethidium (DHE)

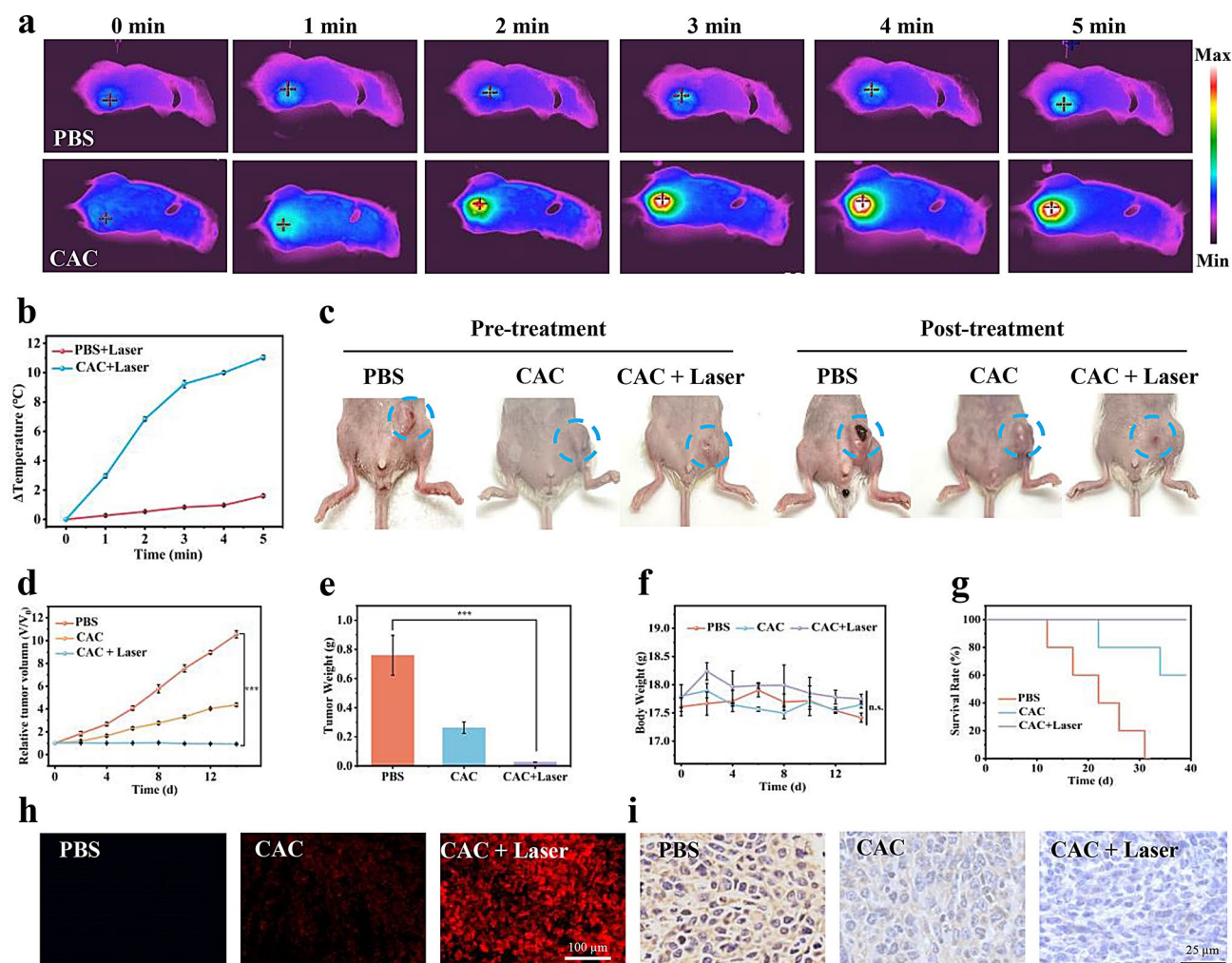


Fig. 7 (a) Infrared thermal images and (b) temperature elevations in the tumors of 4T1 tumor-bearing mice treated with PBS or CAC NPs during 5 min irradiation (1064 nm, 0.75 W/cm²) at 12 h. (c) Representative tumor photographs after treatment with PBS, CAC NPs, and CAC+Laser at predetermined time intervals after different treatments. (10 mg/kg 200 μ L) (d) Tumor volume changes of different groups during treatment, $n=5$. (e) Corresponding tumor weight of different groups during treatment, $n=5$. (f) The body weight changes of tumor-bearing mice with various treatments over 14 days, $n=5$. (g) Survival rates of tumor-bearing mice with various treatments, $n=5$. (h) DHE staining of mouse tumors after 14 days of different treatment to detecting ROS content. Scale bar: 100 μ m. (i) Immunohistochemistry analysis (HSP70) analysis of mouse tumors after 14 days of different treatment. Scale bar: 25 μ m. * $p < 0.05$, ** $p < 0.01$, *** $p < 0.001$

staining. As shown in Fig. 7h, the red fluorescence in the CAC NPs + Laser group was more intense than the other groups, suggesting that the catalytic capability of CAC NPs initiated ROS production. In parallel, the levels of HSP70 protein expression in the CAC NPs + Laser group were almost negligible, which was due to the complete blockage induced by multifunctional nanozyme and the precise MPTT therapeutic time zone guided by ratiometric PA imaging (Fig. 7i). Additionally, the biodistribution and biosafety of the CAC NPs in vivo were elevated through hematological analyses (RBC, WBC, PLT, Gran), standard biochemical (ALT, AST, CREA, BUN) characteristics and H&E staining (heart, liver, spleen, lungs, kidneys). The results revealed that there were no significant abnormalities or lesions in the CAC+Laser group

in comparison with the other groups (Figure S7 and S8), indicating the excellent biocompatibility of CAC NPs. Taken together, based on “one-laser, multi-function” capability, CAC nanoprobe provided a precise space-time mild-temperature photothermal ablation strategy for optimizing the treatment time point and maximizing the synergistic MPTT/PDT/CDT therapy efficacy in breast cancer along with superior biosafety.

Conclusion

In summary, an engineering multifunctional biomimetic nanoprobe CAC was designed and a novel concept of “MPTT therapeutic time zone (t_{MPTT})” was proposed for achieving activatable NIR-II ratiometric PA imaging-guided “targeting-timing” MPTT. CAC NPs were shown

to exhibit superior tumor targeting effects, significant multi-catalytic efficiency, and robust NIR-II light absorption. Subsequent to specific tumor cellular uptake, powerful ·OH generation from CDT amplified oxidative stress, controlled mitochondrial damage and depleted HSP70. Meanwhile, sensitive responsiveness of ABTS make a multiplier gap between the signal intensities of the PA₉₆₀ and PA₇₃₀ to form a ROS ratiometric PA imaging system (PA₇₃₀/PA₉₆₀). In vivo studies indicated that the CAC NPs could be specifically activated in TME with unique enzyme activity, while levels of ROS generation are monitored through ratiometric PA imaging. Based on the comprehensive information provided by activatable ratiometric PA signals, the “MPTT therapeutic time zone (t_{MPTT})” was achievable to acquire optimal MPTT therapeutic performance.

Supplementary Information

The online version contains supplementary material available at <https://doi.org/10.1186/s12951-025-03379-x>.

Supplementary Material 1

Acknowledgements

The authors also would like to thank the shianjia lab (<http://www.shianjia.com>) for the XPS analysis. The authors also acknowledge the Medical Experimental Center of Shanxi Bethune Hospital for providing the necessary equipment for this work.

Author contributions

B. Z. (Conceptualization: Equal; Data curation: Equal; Project administration: Equal; Writing - original draft: Equal). Y. M. (Investigation: Equal; Writing - original draft: Equal). Q.L. (Data curation: Equal; Formal analysis: Equal). S.W., L.C., C.J., and C.H. (Formal analysis: Supporting; Formal analysis: Supporting). H.J. (Conceptualization: Lead). Z.Z., and R.Z. (Conceptualization: Lead; Funding acquisition: Lead; Investigation: Lead; Supervision: Lead; Writing - review & editing: Lead).

Funding

This work has been financially supported by the National Key R&D Program of China (2023YFC3402800), the National Natural Science Foundation of China (82120108016, 82071987, 82372028, 82202238, 82102124), Key Laboratory of Nano-imaging and Drug-loaded Preparation of Shanxi Province (202104010910010), Central Guiding Local Science and Technology Development Fund Projects (YDZJSX20231A054), China Postdoctoral Science Foundation (2023M732142), Shanxi Province Science Foundation for Youths (201901D211343, 202103021223231, 202103021223403, 202203021212100, 202303021212335), Open Fund from Key Laboratory of Cellular Physiology (Shanxi Medical University), Ministry of Education, China (CPOF202215, CPOF202308), Shanxi Province Higher Education “Billion Project” Science and Technology Guidance Project (BYJL053), Key Research and Development Program Project of Shanxi Province (202302130501015).

Data availability

No datasets were generated or analysed during the current study.

Declarations

Ethics approval and consent to participate

All animal operations were approved by the Institutional Animal Care and Use Committee of the Animal Experiment Center of Shanxi Medical University (No. 2016LL141, Taiyuan, China) and followed the National Guidelines for Animal Care.

Consent for publication

Not applicable.

Competing interests

The authors declare no competing interests.

Received: 27 September 2024 / Accepted: 8 April 2025

Published online: 14 May 2025

References

1. Siegel RL, Giaquinto AN, Jemal A. Cancer statistics, 2024. *CA-Cancer J Clin*. 2024;74:12–49.
2. Leon-Ferre RA, Goetz MP. Advances in systemic therapies for triple negative breast cancer. *BMJ*. 2023;381:e071674.
3. Zheng Z, Chen X, Ma Y, et al. Dual H₂O₂-amplified nanofactory for simultaneous self-enhanced nir-ii fluorescence activation imaging and synergistic tumor therapy. *Small*. 2022;18:e2203531.
4. Wang C, Sun Y, Huang S, et al. Self-immolative photosensitizers for self-reported cancer phototheranostics. *J Am Chem Soc*. 2023;145:13099–113.
5. Xiong Y, Rao Y, Hu J et al. Nanoparticle-based photothermal therapy for breast cancer noninvasive treatment. *Adv Mater* 2023; e2305140.
6. Jiang X, Yang M, Fang Y, et al. A photo-activated thermoelectric catalyst for ferroptosis-/pyroptosis-boosted tumor nanotherapy. *Adv Healthc Mater*. 2023;12:e2300699.
7. Li B, Liu H, He Y, et al. A self-checking ph/viscosity-activatable nir-ii molecule for real-time evaluation of photothermal therapy efficacy. *Angew Chem Int Ed Engl*. 2022;61:e202200025.
8. Horton N, Wang K, Kobat D, et al. In vivo three-photon microscopy of subcortical structures within an intact mouse brain. *Nat Photon*. 2013;7:205–9.
9. Koman VB, Bakh NA, Jin X, et al. A wavelength-induced frequency filtering method for fluorescent nanosensors in vivo. *Nat Nanotechnol*. 2022;17:643–52.
10. Zhao M, Li B, Wu Y, et al. A Tumor-Microenvironment-Responsive Lanthanide–Cyanine FRET sensor for NIR-II Luminescence-Lifetime in situ imaging of hepatocellular carcinoma. *Adv Mater*. 2020;32:2001172.
11. Hu K, Xie L, Zhang Y, et al. Marriage of black phosphorus and cu2+ as effective photothermal agents for pet-guided combination cancer therapy. *Nat Commun*. 2020;11:2778.
12. Ding X, Wang T, Bai S, et al. A dual heat shock protein down-regulation strategy using PdA/cu/icg/r controlled by Nir switch enhances mild-photothermal therapy effect. *Adv Healthc Mater*. 2023;12:e2300929.
13. Rosenzweig R, Nillegoda NB, Mayer MP, et al. The hsp70 chaperone network. *Nat Rev Mol Cell Biol*. 2019;20:665–80.
14. Mistrik M, Skrott Z, Muller P, et al. Microthermal-induced subcellular-targeted protein damage in cells on plasmonic nanosilver-modified surfaces evokes a two-phase hsp-p97/vcp response. *Nat Commun*. 2021;12:713.
15. Fang K, Sun Y, Yang J, et al. A dual stimuli-responsive nanoplatform loaded pt(IV)-triptolide prodrug for achieving synergistic therapy toward breast cancer. *Adv Healthc Mater*. 2023;12:e2301328.
16. Wu J, Niu S, Bremner DH, et al. A tumor microenvironment-responsive biodegradable mesoporous nanosystem for anti-inflammation and cancer theranostics. *Adv Healthc Mater*. 2020;9:e1901307.
17. Li R-T, Zhu Y-D, Li W-Y, et al. Synergistic photothermal-photodynamic-chemotherapy toward breast cancer based on a liposome-coated core-shell Aun@nmofs nanocomposite encapsulated with gambogic acid. *J Nanobiotechnol*. 2022;20:212.
18. Whitesell L, Robbins N, Huang DS, et al. Structural basis for species-selective targeting of hsp90 in a pathogenic fungus. *Nat Commun*. 2019;10:402.
19. Ying W, Zhang Y, Gao W, et al. Hollow magnetic nanocatalysts drive starvation–chemodynamic–hyperthermia synergistic therapy for tumor. *ACS Nano*. 2020;14:9662–74.
20. Gürbüz G, Heinonen M. Lc–ms investigations on interactions between isolated β-lactoglobulin peptides and lipid oxidation product malondialdehyde. *Food Chem*. 2015;175:300–05.
21. Chang M, Hou Z, Wang M, et al. Single-atom Pd nanozyme for ferroptosis-boosted mild-temperature photothermal therapy. *Angew Chem Int Ed Engl*. 2021;60:12971–79.
22. Wu S, Gao M, Chen L et al. A multifunctional nanoreactor-induced dual Inhibition of hsp70 strategy for enhancing mild photothermal/chemodynamic synergistic tumor therapy. *Adv Healthc Mater* 2024; e2400819.

23. Lei S, Zhang J, Blum NT, et al. In vivo three-dimensional multispectral photoacoustic imaging of dual enzyme-driven cyclic cascade reaction for tumor catalytic therapy. *Nat Commun.* 2022;13:1298.
24. Zheng Z, Duan A, Dai R, et al. A dual-source, dual-activation strategy for an nir-ii window theranostic nanosystem enabling optimal photothermal-ion combination therapy. *Small.* 2022;18:e2201179.
25. Yang Z, Dai Y, Yin C, et al. Activatable semiconducting theranostics: simultaneous generation and ratiometric photoacoustic imaging of reactive oxygen species in vivo. *Adv Mater.* 2018;30:1707509.
26. Yang Z, Dai Y, Yin C, et al. Activatable semiconducting theranostics: simultaneous generation and ratiometric photoacoustic imaging of reactive oxygen species in vivo. *Adv Mater.* 2018;30:e1707509.
27. Guo B, Yang F, Zhang L, et al. Cuproptosis induced by Ros responsive nanoparticles with elesclomol and copper combined with apd-I1 for enhanced cancer immunotherapy. *Adv Mater.* 2023;35:e2212267.
28. Nguyen LNM, Ngo W, Lin ZP, et al. The mechanisms of nanoparticle delivery to solid tumours. *Nat Rev Bioeng.* 2024;2:201–13.
29. Peng Y, Li M, Jia X, et al. Cu nanoparticle-decorated boron-carbon-nitrogen nanosheets for electrochemical determination of Chloramphenicol. *ACS Appl Mater Inter.* 2022;14:28956–64.
30. Karin E, de Visser JA, Joyce. The evolving tumor microenvironment: from cancer initiation to metastatic outgrowth. *Cancer Cell.* 2023;41(3):374–403.
31. Qu Y, Chu B, Wei X, et al. Cancer-Cell-Biomimetic nanoparticles for targeted therapy of multiple myeloma based on bone marrow homing. *Adv Mater.* 2022;34:2107883.
32. Rao L, Yu GT, Meng QF, et al. Cancer cell Membrane-Coated nanoparticles for personalized therapy in Patient-Derived xenograft models. *Adv Funct Mater.* 2019;29:1905671.
33. Kashif M, Yao H, Schmidt S, et al. Ros-lowering doses of vitamins C and a accelerate malignant melanoma metastasis. *Redox Biol.* 2023;60:102619.
34. Spitz AZ, Zacharioudakis E, Reyna DE, et al. Eltrombopag directly inhibits Bax and prevents cell death. *Nat Commun.* 2021;12:1134.
35. Gao G, Jiang Y-W, Sun W, et al. Molecular targeting-mediated mild-temperature photothermal therapy with a smart albumin-based nanodrug. *Small.* 2019;15:1900501.

Publisher's note

Springer Nature remains neutral with regard to jurisdictional claims in published maps and institutional affiliations.